UC Irvine
UC Irvine Previously Published Works

Title
OBSERVATION OF SMALL-SCALE ANISOTROPY IN THE ARRIVAL DIRECTION DISTRIBUTION OF TeV COSMIC RAYS WITH HAWC

Permalink
https://escholarship.org/uc/item/48x1w7zw

Journal
The Astrophysical Journal, 796(2)

ISSN
0004-637X

Authors
Abeysekara, AU
Alfaro, R
Alvarez, C
et al.

Publication Date
2014-12-01

DOI
10.1088/0004-637x/796/2/108

Peer reviewed

arXiv:1408.4805v2 [astro-ph.HE] 10 Oct 2014

OBSERVATION OF SMALL-SCALE ANISOTROPY IN THE ARRIVAL DIRECTION DISTRIBUTION OF TEV COSMIC RAYS WITH HAWC

A. U. Abeysekara[1,6], R. Alfaro[2], C. Alvarez[3], J. D. Álvarez[4], R. Arceo[3], J. C. Arteaga-Velázquez[4],
H. A. Ayala Solares[5], A. S. Barber[6], B. M. Baughman[7], N. Bautista-Elivar[8], E. Belmont[2], S. Y. BenZvi[10,17],
D. Berley[7], M. Bonilla Rosales[11], J. Braun[7,17], K. S. Caballero-Mora[13], A. Carramiñana[11], M. Castillo[14],
U. Cotti[4], J. Cotzomi[14], E. de la Fuente[15], C. De León[4], T. DeYoung[1], R. Diaz Hernandez[11], J. C. Díaz-Vélez[17],
B. L. Dingus[18], M. A. DuVernois[17], R. W. Ellsworth[19,7], D. W. Fiorino[17,*], N. Fraija[20], A. Galindo[11],
F. Garfias[20], M. M. González[20], J. A. Goodman[7], M. Gussert[21], Z. Hampel-Arias[17], J. P. Harding[18],
P. Hüntemeyer[5], C. M. Hui[5], A. Imran[18,17], A. Iriarte[20], P. Karn[30,17], D. Kieda[6], G. J. Kunde[18], A. Lara[12],
R. J. Lauer[22], W. H. Lee[20], D. Lennarz[23], H. León Vargas[2], J. T. Linnemann[1], M. Longo[21], R. Luna-García[24],
K. Malone[16], A. Marinelli[2], S. S. Marinelli[1], H. Martinez[13], O. Martinez[14], J. Martínez-Castro[24],
J. A. J. Matthews[22], J. McEnery[9], E. Mendoza Torres[11], P. Miranda-Romagnoli[25], E. Moreno[14], M. Mostafá[16],
L. Nellen[26], M. Newbold[6], R. Noriega-Papaqui[25], T. Oceguera-Becerra[15,2], B. Patricelli[20], R. Pelayo[24,31],
E. G. Pérez-Pérez[8], J. Pretz[16], C. Rivière[20,7], D. Rosa-González[11], E. Ruiz-Velasco[2], J. Ryan[27], H. Salazar[14],
F. Salesa Greus[16], A. Sandoval[2], M. Schneider[28], G. Sinnis[18], A. J. Smith[7], K. Sparks Woodle[16],
R. W. Springer[6], I. Taboada[23], P. A. Toale[29], K. Tollefson[1], I. Torres[11], T. N. Ukwatta[1,18], L. Villaseñor[4],
T. Weisgarber[17], S. Westerhoff[17], I. G. Wisher[17], J. Wood[7], G. B. Yodh[30], P. W. Younk[18], D. Zaborov[16],
A. Zepeda[13], and H. Zhou[5]
(The HAWC Collaboration)

Draft version October 13, 2014

ABSTRACT

The High-Altitude Water Cherenkov (HAWC) Observatory is sensitive to gamma rays and charged cosmic rays at TeV energies. The detector is still under construction, but data acquisition with the partially deployed detector started in 2013. An analysis of the cosmic-ray arrival direction distribution based on 4.9×10^{10} events recorded between June 2013 and February 2014 shows anisotropy at the 10^{-4} level on angular scales of about $10°$. The HAWC cosmic-ray sky map exhibits three regions of significantly enhanced cosmic-ray flux; two of these regions were first reported by the Milagro experiment. A third region coincides with an excess recently reported by the ARGO-YBJ experiment. An angular power spectrum analysis of the sky shows that all terms up to $\ell = 15$ contribute significantly to the excesses.

Subject headings: astroparticle physics — cosmic rays

[1] Department of Physics & Astronomy, Michigan State University, East Lansing, MI, USA
[2] Instituto de Física, Universidad Nacional Autónoma de México, Mexico D.F., Mexico
[3] CEFyMAP, Universidad Autónoma de Chiapas, Tuxtla Gutiérrez, Chiapas, Mexico
[4] Universidad Michoacana de San Nicolás de Hidalgo, Morelia, Mexico
[5] Department of Physics, Michigan Technological University, Houghton, MI, USA
[6] Department of Physics & Astronomy, University of Utah, Salt Lake City, UT, USA
[7] Department of Physics, University of Maryland, College Park, MD, USA
[8] Universidad Politécnica de Pachuca, Pachuca, Hidalgo, Mexico
[9] NASA Goddard Space Flight Center, Greenbelt, MD, USA
[10] Department of Physics & Astronomy, University of Rochester, Rochester, NY, USA
[11] Instituto Nacional de Astrofísica, Óptica y Electrónica, Tonantzintla, Puebla, Mexico
[12] Instituto de Geofísica, Universidad Nacional Autónoma de México, Mexico D.F., Mexico
[13] Centro de Investigación y de Estudios Avanzados del Instituto Politécnico Nacional, Mexico D.F., Mexico
[14] Facultad de Ciencias Físico Matemáticas, Benemérita Universidad Autónoma de Puebla, Puebla, Mexico
[15] IAM-Dpto. de Fisica; Dpto. de Electronica (CUCEI), IT.Phd (CUCEA), Phys_Mat. Phd (CUVALLES), Universidad de Guadalajara, Jalisco, Mexico
[16] Department of Physics, Pennsylvania State University, University Park, PA, USA
[17] Wisconsin IceCube Particle Astrophysics Center (WIPAC) & Department of Physics, University of Wisconsin-Madison, Madison, WI, USA
[18] Physics Division, Los Alamos National Laboratory, Los Alamos, NM, USA
[19] School of Physics, Astronomy & Computational Sciences, George Mason University, Fairfax, VA, USA
[20] Instituto de Astronomía, Universidad Nacional Autónoma de México, Mexico D.F., Mexico
[21] Physics Department, Colorado State University, Fort Collins, CO, USA
[22] Department of Physics & Astronomy, University of New Mexico, Albuquerque, NM, USA
[23] School of Physics & Center for Relativistic Astrophysics, Georgia Institute of Technology, Atlanta, GA, USA
[24] Centro de Investigación en Computación, Instituto Politécnico Nacional, Mexico D.F., Mexico
[25] Universidad Autónoma del Estado de Hidalgo, Pachuca, Hidalgo, Mexico
[26] Instituto de Ciencias Nucleares, Universidad Nacional Autónoma de México, Mexico D.F., Mexico
[27] Space Science Center, University of New Hampshire, Durham, NH, USA
[28] Santa Cruz Institute for Particle Physics, University of California, Santa Cruz, Santa Cruz, CA, USA
[29] Department of Physics & Astronomy, University of Alabama, Tuscaloosa, AL, USA
[30] Department of Physics & Astronomy, University of California, Irvine, Irvine, CA, USA
[31] Unidad Profesional Interdisciplinaria de Ingeniería y Tecnologías Avanzadas del Instituto Politécnico Nacional, México, D.F., Mexico

1. INTRODUCTION

The High-Altitude Water Cherenkov (HAWC) Observatory is designed to study the sky in gamma rays and cosmic rays between $50\,\mathrm{GeV}$ and $100\,\mathrm{TeV}$. The detector is currently under construction $4100\,\mathrm{m}$ above sea level at the saddle point between Volcán Sierra Negra and Pico de Orizaba near Puebla, Mexico, at $19°\mathrm{N}$ latitude. HAWC is a water-Cherenkov extensive air-shower array with a wide field of view and nearly 100% duty cycle. With its daily sky coverage of $8.4\,\mathrm{sr}$, HAWC will record both steady and transient gamma-ray sources and provide an unbiased survey of the sky between $-26°$ and $64°$ in declination. While the main targets of HAWC are gamma-ray sources, the detector is also sensitive to cosmic rays. The large number of cosmic rays detected with HAWC forms an undesirable background in the search for gamma-ray sources, but it also permits precise measurements of small deviations from isotropy in the cosmic-ray flux at TeV energies.

Anisotropy in the arrival direction distribution of TeV cosmic rays has been observed with detectors in the Northern and Southern Hemispheres. In the northern sky it has been measured with the Tibet ASγ (Amenomori et al. 2005), Super-Kamiokande (Guillian et al. 2007), Milagro (Abdo et al. 2008, 2009), EAS-TOP (Aglietta et al. 2009), MINOS (de Jong 2011), and ARGO-YBJ (Di Sciascio 2013; Bartoli et al. 2013) experiments. In the Southern Hemisphere, the only measurements come from the IceCube detector (Abbasi et al. 2010, 2011, 2012) and its surface air shower array, IceTop (Aartsen et al. 2013). Observations in the northern and southern sky show qualitatively similar results. In both hemispheres, the anisotropy has components on large angular scales ($> 60°$) and on smaller scales ($< 60°$). The large-scale anisotropy is dominated by an approximately dipole structure with amplitude of order 10^{-3} in relative intensity which persists up to at least 2 PeV (Aartsen et al. 2013), although the dipole phase is observed to change above $100\,\mathrm{TeV}$ (Abbasi et al. 2010; Aglietta et al. 2009). The small-scale structure ranges in relative intensity from several 10^{-4} to 10^{-3}.

The anisotropy in the cosmic-ray flux at these energies is not well-understood. The Larmor radius of a TeV proton in a μG magnetic field is approximately $0.001\,\mathrm{pc}$, orders of magnitude less than the distance to potential astrophysical accelerators, so cosmic rays from these sources should not point back to their origin. It has long been suggested that weak dipole or dipole-like features should be a consequence of the diffusion of cosmic rays from nearby sources in the Galaxy (Erlykin & Wolfendale 2006; Blasi & Amato 2012; Pohl & Eichler 2013; Sveshnikova et al. 2013). It is also possible, though not yet demonstrated, that the magnetic fields of the heliosphere have an influence on the anisotropy (Desiati & Lazarian 2013; Schwadron et al. 2014). The small-scale structure, on the other hand, could be the product of turbulence in the Galactic magnetic field (Giacinti & Sigl 2012; Ahlers 2014) or an additional heliospheric effect (Drury 2013). Several authors have also suggested that the small-scale structure

* dan.fiorino@wipac.wisc.edu

is produced in the decay of quark matter present in pulsars (Perez-Garcia et al. 2014) or in the self-annihilation of dark matter (Harding 2013).

Data acquisition with HAWC started in June 2013, and since then the instrument has accumulated a data set that is already sufficiently large to study cosmic-ray anisotropy at the 10^{-4} level in relative intensity. HAWC data cover a part of the sky that has been extensively studied by the Milagro experiment, which operated near Los Alamos, New Mexico, between 2000 and 2008, and the Tibet ASγ and ARGO-YBJ experiments. HAWC also slightly extends the sky coverage of the previous measurements to declinations as low as $-26°$, observing heretofore uncharted declinations and narrowing the gap in sky coverage between the Northern Hemisphere measurements and those performed with IceCube at the South Pole. The median energy of cosmic rays observed by HAWC in the configuration used in this analysis is $\sim 2\,\mathrm{TeV}$, comparable to Milagro ($1\,\mathrm{TeV}$) and ARGO-YBJ ($1.8\,\mathrm{TeV}$). The actual energy distribution of the events is likely to be more similar in HAWC and ARGO-YBJ, as both detectors are at similar altitude and geomagnetic latitude.

The Milagro cosmic-ray sky map (Abdo et al. 2008) indicates two localized regions of significant cosmic-ray excess called Regions A and B. Region A is roughly elliptical with an angular size of about $15°$, centered at right ascension $\alpha = 69.4°$ and declination $\delta = 13.8°$. Region B is larger, spanning a declination range $15° < \delta < 50°$ at right ascension $\alpha \simeq 130°$. The relative intensity in Regions A and B is 6×10^{-4} and 4×10^{-4}, respectively. Both regions have also been observed with the Tibet ASγ and ARGO-YBJ experiments. In a recent study based on 3.7×10^{11} events (Bartoli et al. 2013), the ARGO-YBJ experiment presented evidence for two additional excess regions with lower relative intensity than Regions A and B. Region 3 in the ARGO-YBJ map is a rather elongated structure around $\alpha = 240°$, spanning the declination range $15° < \delta < 55°$, with a maximum relative intensity of 2.3×10^{-4}. Another new region (Region 4) around $\alpha = 210°$ and $\delta = 30°$ has a maximum relative intensity of 1.6×10^{-4} and is currently the weakest statistically significant excess in the ARGO-YBJ map.

In this paper, we present the results of a search for cosmic-ray anisotropy in the northern sky with HAWC. With current statistics, the HAWC cosmic-ray sky map exhibits three regions of significantly enhanced flux. The two strongest excess regions coincide with Milagro Regions A and B (ARGO-YBJ Regions 1 and 2). The location and relative intensity of the largest excess in Region A in HAWC and Milagro data show some differences, but the excess observed with HAWC agrees well with the excess seen by ARGO-YBJ. A third significant excess in the HAWC map coincides with Region 4 in the ARGO-YBJ map. With HAWC, this region is detected at almost twice the relative intensity observed by ARGO-YBJ, making it more significant in HAWC despite the considerably shorter observation period. A small excess in the HAWC map near Region 3 is currently not statistically significant.

In addition to the arrival direction distribution, we also present the angular power spectrum of the cosmic rays. This analysis confirms the presence of a strong dipole and quadrupole moment and shows significant power on

angular scales down to 12° with current statistics. The power spectrum can be compared to the spectrum of the southern sky (Abbasi et al. 2011) and to recent model predictions that link the presence of higher order multipoles to the dipole component using phase-space arguments (Ahlers 2014).

The paper is organized as follows. After a brief description of the HAWC detector (Section 2), we describe the data set used in this analysis (Section 3). In Section 4, we present the arrival direction distribution, an analysis of the excess regions, and the results of the angular power spectrum analysis. The paper is summarized in Section 5.

The paper focuses on the measurement of the small-scale anisotropy. With less than a full year of coverage, we expect that large-scale anisotropy measurements are still contaminated by several effects that typically cancel with one or more full years of continuous data, such as the dipole produced by the motion of the Earth around the Sun. The measurement of the large-scale anisotropy with HAWC will be the subject of a future publication.

2. THE HAWC DETECTOR

The Earth's atmosphere is not transparent to cosmic rays and gamma rays at TeV energies. The incoming primary particle interacts with a molecule in the atmosphere and creates an extensive air shower, a huge cascade of secondary particles. Ground-based detectors like HAWC need to reconstruct the properties of the incoming cosmic rays from the particles of the shower cascade that reach the observation level. In HAWC, the secondary particles of the air shower cascade are detected with instrumented water tanks, making use of the fact that the relativistic particles of the shower cascade produce Cherenkov light when traversing the water in the tanks.

The HAWC Observatory (Abeysekara et al. 2013b) is a $22,000\,\mathrm{m}^2$ array of close-packed water Cherenkov detectors (WCDs). Each WCD consists of a cylindrical steel water tank 4.5 m in height and 7.3 m in diameter. A black plastic liner inside each tank contains 188,000 liters of purified water, and four photo-mulitplier tubes (PMTs) are attached to the liner on the floor of the tank: one central high-quantum efficiency Hamamatsu 10" R7081 PMT and three Hamamatsu 8" R5912 PMTs each at 1.8 m from the center forming an equilateral triangle. The PMTs face upward to observe the Cherenkov light produced when charged particles from air showers enter the tank. When construction is complete, the observatory will comprise 300 water Cherenkov detectors with 1200 PMTs.

The signals from each PMT are transferred via RG59 coaxial cables to a counting house in the center of the array where the pulses are amplified and shaped using custom front-end electronics. The shaped pulse is compared with two different discriminator levels, and the time over each level, high and low time over threshold (ToT), are recorded as time-stamped edges with 100 ps resolution using CAEN VX1190A TDC modules. The shaping is such that ToT values are proportional to the logarithm of the charge in the pulse.

Once the signals have been time-stamped the data are aggregated into an online data stream. Multiple online clients pull data from Single Board Computers that poll the TDCs for data, combine the data into blocks, and
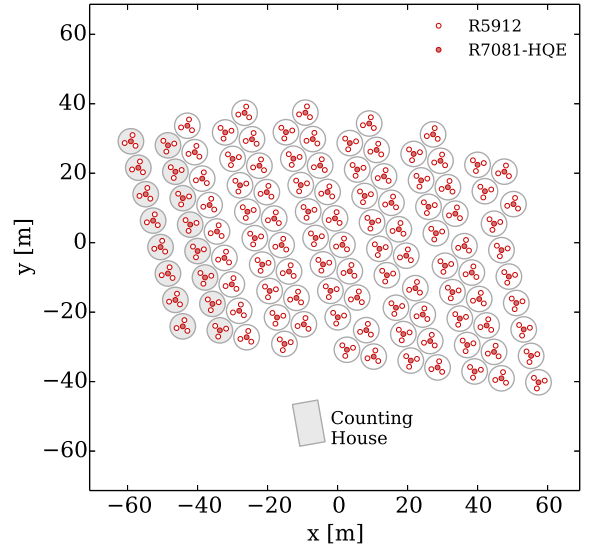

Figure 1. Layout of HAWC-95, with large shaded circles indicating the additional two rows of tanks present in HAWC-111. The positions of the 8" R5912 PMTs are shown as small open circles and the 10" R7081 high-quantum efficiency PMTs are shown as small filled circles.

buffer them for readout. The hits are sorted into an ordered time series, and a simple multiplicity trigger is applied to identify candidate air shower events. The trigger condition requires at least 15 PMTs to be above threshold within a sliding time window of 100 ns. The triggered events are then written to disk. As the data are being saved, an online reconstruction determines the arrival direction of the primary particle in real time. However, since the detector has been growing and changing, in this analysis the angular reconstruction was performed offline.

The hit times are calibrated to remove both a relative timing offset due to differences between individual PMT responses and a timing offset from the distribution of arrival times expected in an air shower (Abeysekara et al. 2013b). The relative timing offset, or slewing offset, is the result of the combined response time of a specific PMT and the front-end electronics. The slewing offsets are determined with an on-site laser calibration system that sends pulses of varying intensities to each WCD while on-site computers record the PMT responses. After accounting for the relative timing difference between PMTs, the timing offset between a best-fit air shower front and the PMT hit times is calculated and subtracted in an iterative shower reconstruction procedure.

3. THE DATA SET

The analysis in this paper uses data recorded between June 16, 2013, and February 27, 2014. Before August 12, 2013 the detector was operated with 95 tanks (HAWC-95), and afterwards with 111 tanks (HAWC-111). The layout of HAWC-95 and HAWC-111 is shown in Fig. 1.

For all analyses described in this paper, we apply additional cuts to improve the data quality. To remove poorly reconstructed events, we require at least 30 triggered PMTs per event. The remaining events have a median angular resolution of 1.2° and a median energy of 2 TeV according to the detector simulation, which
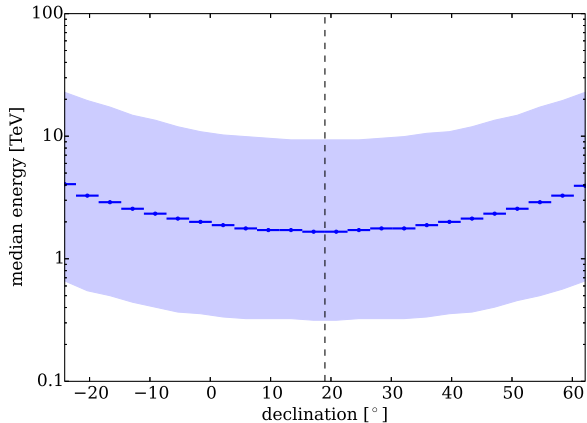
Figure 2. Median energy of the cosmic-ray flux observed in HAWC as a function of declination. The dashed line indicates the latitude of the detector, and the shaded region corresponds to a 68% containing interval.

Figure 3. Relative intensity of the cosmic-ray flux in a sky map centered on the position of the Moon. $\Delta\alpha$ and $\Delta\delta$ are the right ascension and declination of the cosmic rays with respect to the right ascension and declination of the Moon. The Moon shadow is shown for 113 days of HAWC-95/111 data. The deficit corresponds to a significance of $24\,\sigma$.

uses the CORSIKA code (Heck et al. 1998) to generate air showers in combination with a Geant4-based simulation (Agostinelli et al. 2003) of the detector response. The angular resolution for cosmic-ray showers derived from simulations agrees with the estimate from the observation of the cosmic-ray shadow of the Moon, which is described in this section. The completed array is expected to have an angular resolution of about $0.2°$ for gamma rays above $2\,\text{TeV}$ (Abeysekara et al. 2013a). Gamma rays are present in this dataset but the gamma ray population is negligible with respect to cosmic rays. The significance of the gamma-ray background in this analysis will be the subject of future work.

The median energy quoted above refers to the total cosmic-ray flux detected with HAWC. For localized excess regions, which are the main interest of this paper, the median energy is a function of the region's declination. The dependence of the median energy on declination is shown in Fig. 2, together with the central 68% quantile. The median cosmic-ray energy ranges from $1.7\,\text{TeV}$ at a declination of $19°$ to $4\,\text{TeV}$ at declinations below $-20°$ and above $60°$, near the border of the field of view.

The data are further reduced by requiring that only full and continuous sidereal days of data runs be used. This produces a nearly uniform exposure across right ascension, providing for an easy interpretation of the significance map since exposure changes only in declination. The only non-uniformity in right ascension is the result of diurnal variations in the cosmic-ray rate. This has been confirmed using a set of simulated data with an event time distribution that matches the actual distribution.

During most of HAWC-95, construction took priority over data-taking and, while data-taking is largely uninterrupted in the HAWC-111 data set, many HAWC-111 data runs do not last a full sidereal day due to detector upgrades and tests of the data acquisition and calibration systems. As the procedures for upgrades and calibration of the detector are improved and construction ceases, the number of full sidereal days will approach the number of days of detector up-time.

The resulting data set contains 113 full and continuous sidereal days during which the detector collected
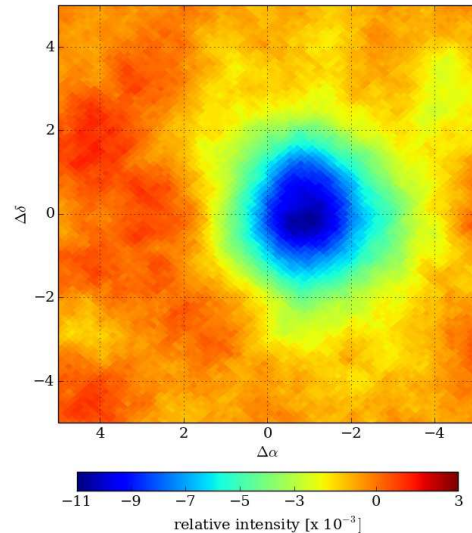
4.9×10^{10} well-reconstructed events - about 1.5 times the number of events in the IceCube 2009-2010 anisotropy data set (Abbasi et al. 2011), but still four times smaller than the total number of Milagro events (Abdo et al. 2008) and almost 8 times smaller than the number of ARGO-YBJ events (Bartoli et al. 2013).

The angular resolution for cosmic rays and the energy of the isotropic cosmic-ray flux triggering HAWC can be verified by studying the cosmic-ray shadow of the Moon. The Moon produces an observable deficit in the nearly isotropic flux of cosmic-ray air showers incident at Earth, and the width and shape of the deficit indicate the instrument's point-spread function for cosmic rays. The apparent position of the Moon shadow differs from its true position because of deflections of the cosmic rays in the geomagnetic field. From simulations described in detail in Abeysekara et al. (2013c), the geomagnetic deflection $\delta\theta$ of particles arriving at the HAWC altitude and geographic location can approximately be summarized by

$$\delta\theta \simeq 1.6° \cdot Z \left(\frac{E}{\text{TeV}} \right)^{-1} \,, \qquad (1)$$

where E and Z are the cosmic-ray energy and charge, respectively.

HAWC-111 observes the shadow of the Moon at a significance of $13\,\sigma$ per month. To study the location and shape of the deficit, we produce sky maps centered on the position of the Moon. The relative intensity of the cosmic-ray flux as a function of the relative right ascension $\Delta\alpha$ and declination $\Delta\delta$ is shown in Fig. 3 and was obtained by subtracting the calculated equatorial coordinates of the Moon $(\alpha_{\text{Moon}}, \delta_{\text{Moon}})$ from the right ascension α and declination δ of each reconstructed cosmic-ray shower. In 113 days of HAWC-95/111 data, the statistical significance of the deficit in the cosmic-ray flux is about $24\,\sigma$.

From a fit of a two-dimensional Gaussian to the deficit region, we find that the observed Moon shadow is offset by $-1.05° \pm 0.05°$ in $\Delta\alpha$ and $-0.02° \pm 0.06°$ in $\Delta\delta$ and has a width of $1.26° \pm 0.05°$. According to simulations, the cosmic-ray deflection in the magnetic field also leads to a slight broadening of the width of the Moon shadow, so it should be interpreted as an upper limit on the angular resolution of the detector. The shift of the shadow indicates that the observed energies are dominated by proton-initiated showers of about $1.6\,\mathrm{TeV}$. Both angular resolution and energy scale are consistent with the predictions from simulations.

4. ANALYSIS

4.1. *Relative Intensity and Significance Map*

The search for anisotropy is based on techniques described in Abdo et al. (2008) and Abbasi et al. (2011). To produce a sky map of the relative intensity of the cosmic-ray flux requires a comparison of the data to a reference map which represents the response of the detector to an isotropic cosmic-ray flux. This reference map is not itself isotropic, as atmospheric effects cause diurnal changes in the cosmic-ray rate and the asymmetric shape of the HAWC-95/HAWC-111 tank configuration leads to an uneven event distribution in right ascension. Because the reference map needs to account for these and other effects, which are difficult or impossible to simulate at the required level of accuracy, it has to be constructed from the data themselves.

We begin by binning the sky into an equal-area grid in equatorial coordinates with an average pixel size of $0.23°$ using the HEALPix library (Gorski et al. 2005). The resolution of the HEALPix pixelation of the sphere is defined by a parameter N_{side} which is related to the number of pixels by $N_{\mathrm{pix}} = 12\,N_{\mathrm{side}}^2$. In this analysis, we chose $N_{\mathrm{side}} = 256$, so the sky is originally divided into $786\,432$ pixels[1]. Since HAWC covers the sky at declinations between $-26°$ and $64°$, the total number of independent pixels is $525\,716$.

A binned data map $N(\alpha, \delta)$ is used to store the arrival directions of air showers reconstructed from data. The reference map $\langle N(\alpha, \delta) \rangle$ is produced using the direct integration technique described in Atkins et al. (2003), adapted for the HEALPix grid. We begin by collecting all events recorded during a predefined time period Δt and convolve the local arrival direction distribution with the detector event rate. The method effectively smooths out the true arrival direction distribution in right ascension on angular scales of roughly $\Delta t \cdot 15°\,\mathrm{hour}^{-1}$, so the analysis is only sensitive to structures smaller than this characteristic angular scale. The direct integration method produces a reference map with the same underlying local arrival direction distribution and the same event rate as the data. Therefore, any effects from temporal variations in the cosmic-ray rate or from the detector geometry appear in the data map as well as in the reference map and cancel when the two are compared to produce maps of significance or relative intensity. The relative intensity map is calculated as

$$\delta I(\alpha_i, \delta_i) = \frac{\Delta N_i}{\langle N \rangle_i} = \frac{N(\alpha_i, \delta_i) - \langle N(\alpha_i, \delta_i) \rangle}{\langle N(\alpha_i, \delta_i) \rangle}, \quad (2)$$

[1] For the analysis of the Moon shadow in Section 3, $N_{\mathrm{side}} = 512$ was used.

which gives the amplitude of deviations from the isotropic expectation in each angular bin i.

We emphasize that this algorithm estimates the reference level by averaging the number of events over a fixed declination band. Because different declination bands have different normalizations, the method is not sensitive to anisotropy that depends only on declination, *i.e.*, with constant relative intensity in right ascension. Studies using simulated data (Santander 2013) show that this does not affect typical small-scale structure, but it reduces the sensitivity of the method to large-scale structure. As an example, for a pure dipole tilted at some angle with respect to the equatorial plane, the method is only sensitive to the *projection* of the dipole onto the equatorial plane.

To improve the sensitivity to features on angular scales larger than the pixel size, we apply a smoothing procedure which takes the event counts in each pixel and adds the counts from neighboring pixels within a radius θ. This is equivalent to convolving the map with a top hat function of radius θ. Applied to both the data map and the reference map, the procedure leads to maps with the original binning, but neighboring pixels are no longer independent and pixel values become highly correlated over a range θ. In this paper, we use $\theta = 10°$, the same scale used in Abdo et al. (2008). This scale is a compromise, since the optimal θ varies from region to region, with no single scale appropriate for the entire sky map. However, $\theta = 10°$ displays all the relevant features and allows us to analyze the shape of the anisotropy.

Gamma rays are present in the data set, but since the analysis is not optimized for gamma rays and we apply a smoothing radius of $10°$, far larger than the optimal smoothing radius for point sources, even the brightest TeV gamma-ray sources, such as the Crab, do not appear as a significant excess in the smoothed maps.

The significance of the deviation of the data from the isotropic expectation in each bin is calculated using the method described in Li & Ma (1983). In this method, the statistical uncertainty of the number of events in each bin of the reference map depends on the quantity $\alpha_{\mathrm{Li\text{-}Ma}}$, the ratio of time spent on-source to time spent off-source. The effective value for $\alpha_{\mathrm{Li\text{-}Ma}}$ depends on the integration time Δt, smoothing radius θ, and declination δ and is calculated using

$$\alpha_{\mathrm{Li\text{-}Ma}} = \frac{\pi\,\theta^2}{2\,\theta\,(15°/\mathrm{hr})\,\Delta t\,\cos\delta}\,. \quad (3)$$

For $\Delta t = 24\,\mathrm{h}$, $\theta = 10°$, and $\delta = 0°$, the value for $\alpha_{\mathrm{Li\text{-}Ma}}$ is 0.0436.

Direct integration requires the local arrival direction distribution and thus the acceptance of the detector to be stable throughout the time period Δt. Using a χ^2-difference test to compare local arrival direction distributions over various time periods, we find that the shape of these distributions is stable over very long periods (up to several weeks) and changes only when the detector geometry changes (for example at the time of the switch from HAWC-95 to HAWC-111). The high stability of the detector allows us to use $\Delta t = 24\,\mathrm{h}$ in this analysis. As described above, this value preserves features on all angular scales, including the dipole moment. The angular power spectrum can be determined directly from this relative intensity map (see Section 4.3).
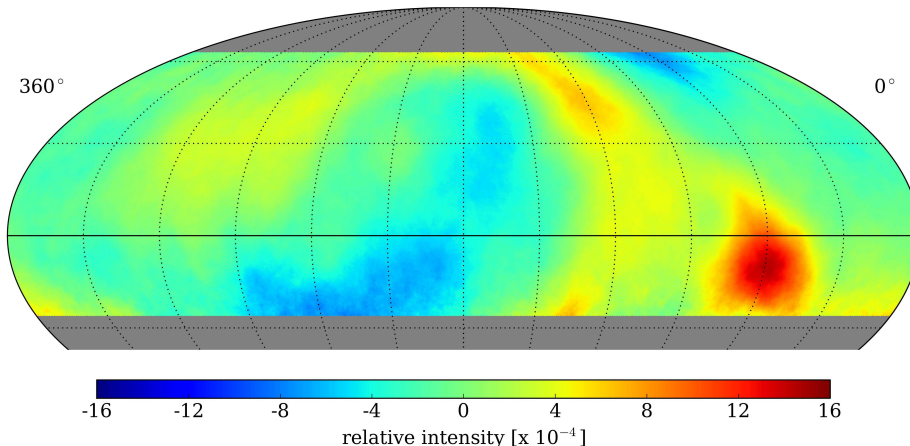
Figure 4. Relative intensity of the cosmic-ray flux for 113 days of HAWC-95/111, in equatorial coordinates. Right ascension runs from $0°$ to $360°$ from right to left. The solid horizontal line denotes a declination of $0°$. Lines of equal right ascension and declination are separated by $30°$. The map contains 4.9×10^{10} events. An integration time of $\Delta t = 24\,\mathrm{h}$ is used to access the largest features present in the map. The map is shown with $10°$ smoothing applied.

The relative intensity of the cosmic-ray flux for an integration time of $\Delta t = 24\,\mathrm{h}$ and a smoothing scale $\theta = 10°$ is shown in Fig. 4. Several significant features appear in this map. The localized excess region at right ascension $60°$ and declination $-10°$, which roughly coincides with Region A of the Milagro map and (more accurately) with Region 1 of the ARGO-YBJ map, dominates the sky map. In addition, the large-scale structure of the cosmic-ray flux, with its broad deficit region at $200°$, is clearly visible in this map. The large-scale structure potentially distorts any smaller structures, enhancing their excess in the region near the maximum of the large-scale structure and suppressing them near the broad minimum. As we are interested in structure on scales smaller than $60°$, corresponding to multipoles $\ell > 3$, we need to remove the lower order multipoles from the sky map. We apply two different methods to remove or suppress the $\ell \leq 3$ term.

In the first method, we directly fit the relative intensity map to the sum of the monopole $(\ell = 0)$, dipole $(\ell = 1)$, quadrupole $(\ell = 2)$, and octupole $(\ell = 3)$ terms of an expansion in Laplace spherical harmonics $Y_{\ell m}$. The fit function $F(\alpha, \delta)$ therefore has the form

$$F(\alpha_i, \delta_i) = \sum_{\ell=0}^{3} \sum_{m=-\ell}^{\ell} a_{\ell m} Y_{\ell m}(\pi - \delta_i, \alpha_i) \ , \qquad (4)$$

where (α_i, δ_i) are the right ascension and declination of the ith pixel and the $a_{\ell m}$ are the 16 free parameters of the fit. We then subtract the fit result from the map, and analyze the residual map.

We perform the fit on the $525\,716$ pixels of the relative intensity map that lie in the field of view of HAWC. The $\chi^2/\mathrm{ndf} = 527\,282/525\,700$ corresponds to a χ^2-probability of 6.0%. The marginal probability indicates that additional smaller structure is still present in the data. Note that this fit gives a significantly better result than the fit with $\ell_{\max} = 2$ only (DC offset + dipole + quadrupole), corresponding to a χ^2-difference of 262 with 7 degrees of freedom. The residual map in relative

intensity (top) and significance (bottom) are shown in Fig. 5.

The second method uses a shorter integration time, $\Delta t = 4\,\mathrm{h}$, to filter any structure with angular extent greater than $60°$. In Fig. 6, we show the relative intensity (top) and significance maps (bottom) produced with this method. A comparison between Fig. 5 and Fig. 6 shows that the maps are largely equivalent. While regions A and C agree well in shape and relative intensity, region B extends into mid-latitudes for the $\Delta t = 4\,\mathrm{h}$ map.

There are also regions of strong deficits visible, typically on both sides of the strong excess regions. The appearance of these deficit regions, correlated with the excess regions, is a well-known artifact of the method (Abdo et al. 2008). They appear because the background near strong excesses is overestimated due to the fact that the excess events are part of the background estimation.

The two methods to remove the large-scale anisotropy are affected by different systematic uncertainties. Estimating the background using $\Delta t = 24\,\mathrm{h}$ and explicitly subtracting lower order multipoles should, in principle, minimize artifacts from the presence of strong excesses described above. However, because of the incomplete sky coverage, the removal of the lower order multipoles can potentially affect higher order terms, too. This effect is studied with the angular power spectrum analysis described in Section 4.3 and is found to be small in HAWC data. Filtering the low order multipoles by choosing a short integration time Δt also influences higher order multipoles (in a less transparent way than the direct subtraction), and it depends on the choice of Δt.

In the following analysis, we estimate the systematic error on the relative intensity of cosmic-ray excess regions by comparing the intensity obtained with the two methods, and, in addition, by comparing two different integration times (3 h and 4 h) which are both found to preserve the power in the higher order multipoles of the angular power spectrum (Section 4.3). The larger difference of the two alternative methods is taken as the systematic uncertainty reported in Section 4.2 for the various regions
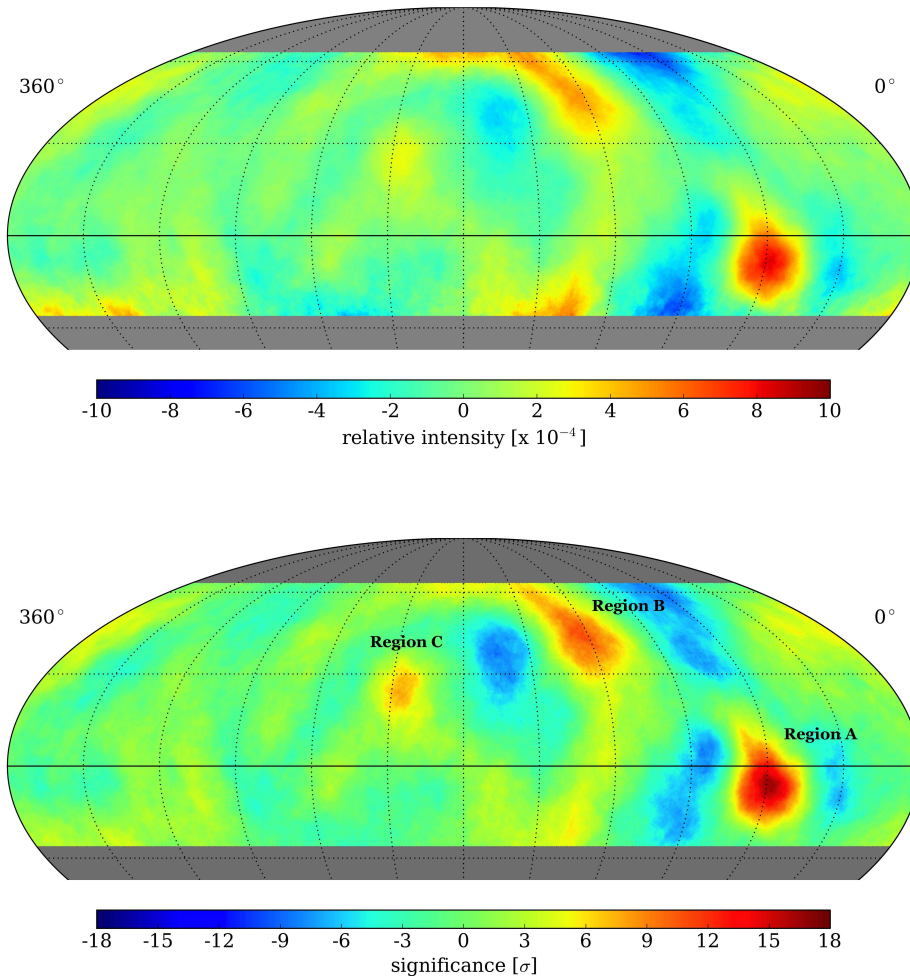
Figure 5. Relative intensity *(top)* and pre-trial significance *(bottom)* of the cosmic-ray flux after fit and subtraction of the dipole, quadrupole, and octupole term from the map shown in Fig. 4. The map is shown with 10° smoothing applied.

of excess. The cosmic-ray dipole caused by the motion of the Earth around the Sun can potentially distort any sidereal large-scale structure, but should have no effect on the small-scale structure.

4.2. Results and Discussion

After the elimination of the large-scale structure, the residual HAWC cosmic-ray sky map shows several prominent features, notably three regions of excess flux with high significance. The strongest excess, with a pre-trial significance of $17.0\,\sigma$, is found at $\alpha = 57.5°$ and $\delta = -6.3°$ and corresponds to Region A in the Milagro sky map and Region 1 in the ARGO-YBJ sky map. The relative intensity of the excess in this region peaks at $(8.5\pm0.6\pm0.8)\times10^{-4}$, where the first error is statistical and the second error is systematic. A detailed map of the morphology of this region is shown in the left panel of Fig. 7. The median cosmic-ray energy at this declination is 2.1 TeV. For comparison, we also fit a two-dimensional Gaussian function to the relative intensity map around Region A. The center is located at $\alpha = 60.0° \pm 0.7°$ and $\delta = -7.1°\pm0.8°$, with an amplitude of $(10.1\pm1.2)\times10^{-4}$. The width is $7.1°\pm1.3°$ in right ascension and $7.8°\pm1.3°$

in declination.

The location and relative intensity of Region A in the HAWC sky map are consistent with the ARGO-YBJ measurement, but there are notable differences compared to Milagro. The peak relative intensity in HAWC is a factor of 1.5 higher than in Milagro, but the locations of the peaks also differ. While the HAWC excess extends up to $\delta = 15°$, the most significant peak is observed in the Southern Hemisphere at $\delta = -6.3°$, at the edge of the field of view of Milagro. At the location of the centroid of Milagro's Region A, the relative intensity in HAWC is only $(1.5\pm0.4)\times10^{-4}$, a factor of 4 smaller than the Milagro excess. A possible reason for this discrepancy is that the median energy of the Milagro data is higher than in HAWC and that the upper part of Region A, where Milagro observes the largest excess, is brighter at higher energies. The energy dependence of the Region A excess will be studied in more detail in Section 4.4.

Because of its more southerly latitude (19°N) compared to Milagro (36°N) and ARGO-YBJ (30°N), HAWC observes the lower part of Region A at a more favorable zenith angle. This can account for the fact that the significance of Region A in HAWC is already as
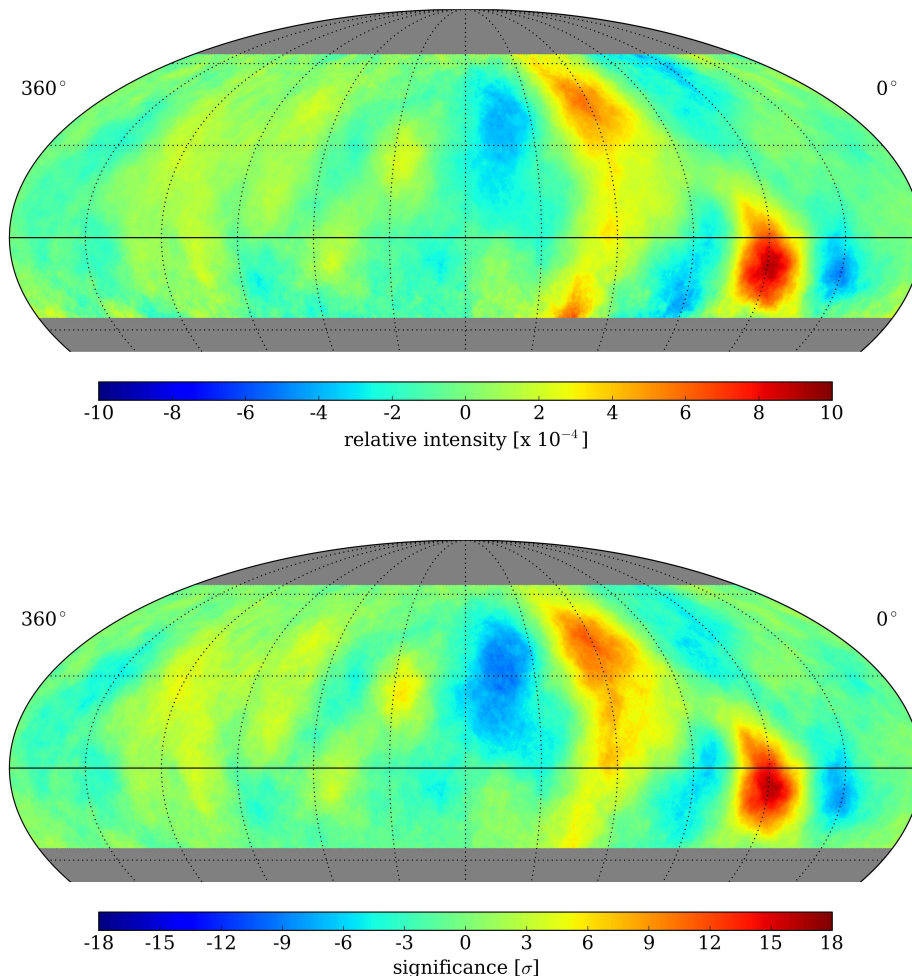
Figure 6. Relative intensity *(top)* and pre-trial significance *(bottom)* of the cosmic-ray flux using a background estimated from direct integration with a time period $\Delta t = 4\,$h. The map is shown with $10°$ smoothing applied.

strong as in Milagro even though the HAWC data set is still considerably smaller.

The elongated excess around $\alpha = 120°$, identified as Region B in the Milagro map and Region 2 in the ARGO-YBJ map, extends over a wide range of declinations. It is most significant at $(122.1°, 43.8°)$ with a pre-trial significance of $11.2\,\sigma$ and a relative intensity of $(5.2 \pm 0.6 \pm 0.7) \times 10^{-4}$. The morphology of this region is shown in the center panel of Fig. 7.

There is considerable uncertainty in the shape of Region B. It appears as two separate regions in Fig. 5, one at high northern latitude and one at declination $\delta < 0°$. The two regions are connected by band-like structure with lower relative intensity. The map produced with an integration time of $\Delta t = 4\,$h (Fig. 6) also shows these regions, but the shape of the upper region is broader and the intensity of the connecting band is brighter. Region B essentially spans almost the entire declination range visible to HAWC. It is also the only small-scale excess observed by a detector in the Northern Hemisphere that appears to continue into the sky regions accessible to Ice-Cube, although the excess identified as Region 1 in the IceCube skymap (Abbasi et al. 2011) is shifted to slightly

lower right ascension $(122.4°)$.

A third excess region, Region C in Fig. 5, is centered at $\alpha = 205.7°$ and $\delta = 22.5°$ with a pre-trial significance of $8.2\,\sigma$ and a peak relative intensity of $(2.9 \pm 0.4 \pm 0.5) \times 10^{-4}$. This excess region is not significant in the Milagro data, but the ARGO-YBJ collaboration has observed a hot spot at the same location, called Region 4 in Bartoli et al. (2013). The morphology of this region is shown in the right panel of Fig. 7. The median cosmic-ray energy at this declination is $2.0\,$TeV.

Region C is located at the center of the minimum of the large-scale structure, but it is already visible (albeit with smaller significance) in Fig. 4 before the subtraction of the $\ell \leq 3$ terms. The relative intensity of this region in HAWC is a factor of 1.8 higher than reported by ARGO-YBJ.

The significances quoted for the three excess regions do not account for statistical trials caused by the search for any significant deviation from isotropy in the $525\,716$ pixels. In a blind search we would account for "look elsewhere" effects by repeating the analysis for a large number of isotropic sky maps with the same exposure as the data. Because such a calculation is computation-
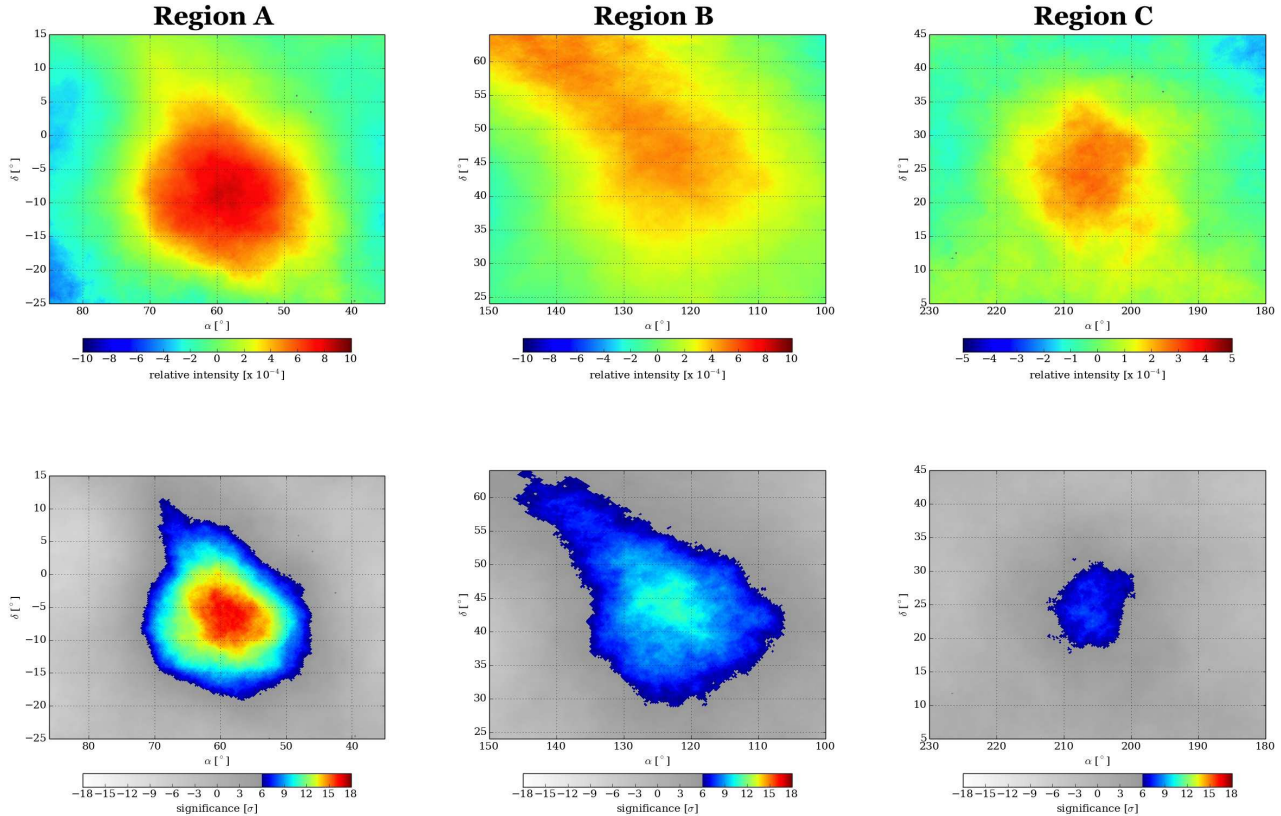
Figure 7. Relative intensity *(top row)* and pre-trial significance *(bottom row)* of the cosmic-ray flux in the vicinity of Region A *(left)*, Region B *(center)*, and Region C *(right)*, from the map shown in Fig. 5.

ally prohibitive given the high pre-trial significance of the excess regions, we conservatively estimate that the number of independent pixels in the sky map is of order 10^5. In fact, the trials penalty is much smaller because we are not performing a blind search of the data; these excess regions have been observed by other experiments. However, even with a correction factor of 10^5, the significances of Regions A, B, and C are 16.1σ, 10.2σ, and 6.7σ after trials, respectively.

The ARGO-YBJ experiment has also observed a new region with a maximum relative intensity of 2.3×10^{-4}, called Region 3 in Bartoli et al. (2013), which is a factor of 1.4 more intense than the excess in Region C. The shape of this new region is rather complex. The most intense signal is found near $\alpha = 240°$ and $\delta = 45°$, although the region extends to declinations as low as $15°$. While this region is brighter in ARGO-YBJ than Region C, it is currently not significant in HAWC data; the largest pre-trial significance within $10°$ of the ARGO-YBJ peak excess is $3.7\,\sigma$. This region will be studied in more detail with a larger data set in the future.

4.3. *Power Spectrum Analysis*

A common tool to search for correlations between bins in a map without prior knowledge of the expected angular scale of excess or deficit regions is the angular power spectrum. The amplitude of the power spectrum at multipole order ℓ is correlated with the presence of structure at angular scales $180°/\ell$. We perform an angular power spectrum analysis on the unsmoothed relative intensity

map $\delta I = \Delta N/\langle N\rangle$. In this analysis, δI is treated as a scalar field which is expanded in terms of a basis

$$\delta I(\alpha_i, \delta_i) = \sum_{\ell=0}^{\infty} \sum_{m=-\ell}^{\ell} a_{\ell m} Y_{\ell m}(\pi - \delta_i, \alpha_i) \quad , \qquad (5)$$

where the $Y_{\ell m}$ are the real (Laplace) spherical harmonics and the $a_{\ell m}$ are the multipole coefficients of the expansion in the sky map. The power spectrum of the relative intensity is defined as the variance of the multipole coefficients $a_{\ell m}$,

$$\mathcal{C}_\ell = \frac{1}{2\ell+1} \sum_{m=-\ell}^{\ell} |a_{\ell m}|^2 \quad . \qquad (6)$$

Due to the partial sky coverage of HAWC, the Y_{lm} do not form an orthonormal basis and the true power spectrum cannot be calculated directly. Following the approach outlined in detail in Abbasi et al. (2011), we first calculate the so-called pseudo-power spectrum, a convolution of the power spectrum of the data and the power spectrum of the corresponding relative exposure map. We use the publicly available PolSpice software (Szapudi et al. 2001; Chon et al. 2004) to calculate the true power spectrum from the pseudo-power spectrum.

The angular power spectrum of the unsmoothed relative intensity map is shown in Fig. 8. The blue and red points show the power spectrum before and after the subtraction of the $\ell \leq 3$ terms. The error bars are calculated
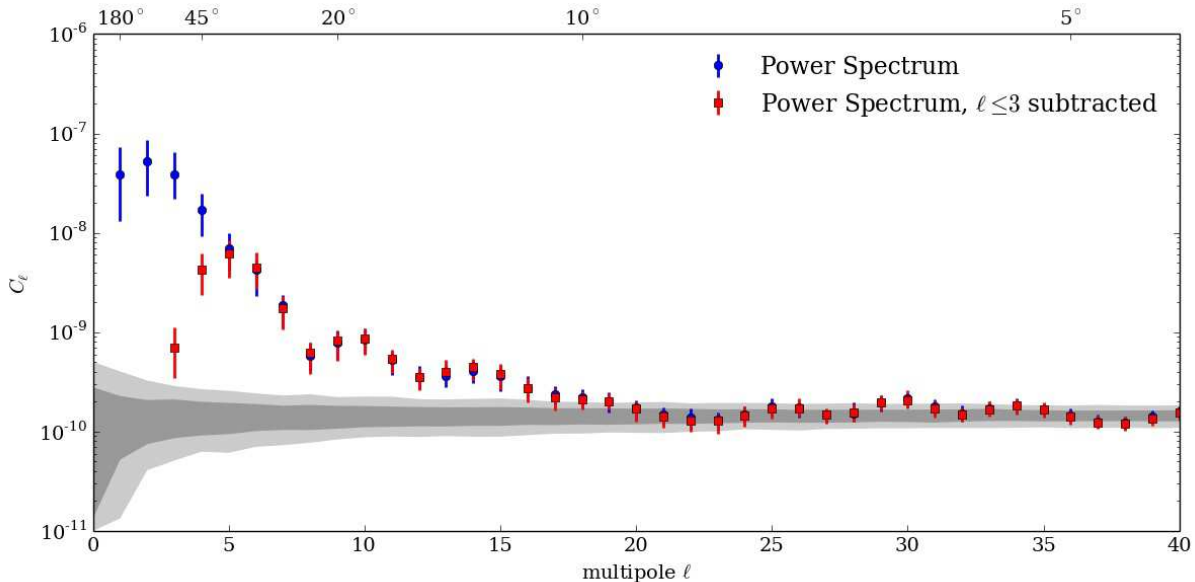
Figure 8. Angular power spectra of the unsmoothed relative intensity map (Fig. 4) before (blue) and after (red) fitting and subtraction of the dipole, quadrupole, and octupole moments ($\ell \leq 3$). The error bars on the C_ℓ are statistical. Note that the $\ell < 3$ terms in the residual spectrum are not shown because they were found to be compatible with zero within statistical uncertainties. The gray bands show the 68% and 95% spread of the C_ℓ for isotropic data sets.

from the diagonal components of the covariance matrix (see Efstathiou (2004) for a detailed discussion). The gray bands in Fig. 8 indicate the 68% and 95% spread of the C_ℓ around the median for a large number of relative intensity maps representing isotropic arrival direction distributions. These isotropic skymaps were generated by comparing the counts from the reference map to a Poisson-fluctuated reference map.

The angular power spectrum of the relative intensity map shows, as expected, a strong dipole ($\ell = 1$) and quadrupole ($\ell = 2$) moment. With increasing ℓ, the strength of the corresponding moments C_ℓ decreases, but higher order multipoles up to $\ell = 15$ still contribute significantly to the sky map. After subtraction of the dipole, quadrupole, and octupole ($\ell = 3$) moments by the fit method described above, the dipole and quadrupole moments are missing in the spectrum and the octupole moment is diminished by two orders of magnitude. All other moments are still present and, excluding $\ell = 4$, have the same strength as in the original map given statistical uncertainties. This indicates that the procedure described above is successful in reducing the correlation between the different ℓ modes caused by the incomplete sky coverage. However, the fact that the octupole moment is not completely removed after the fit shows that some correlation between modes persists.

As mentioned in Section 4.1, sky maps produced with the direct integration method to estimate the reference level are potentially biased because the method can mask or reduce the strength of declination-dependent structures. Since the angular power spectrum is based on these sky maps, it is also affected by this limitation of the technique. The effect can lead to an underestimation of the power in certain multipoles, especially those with low ℓ, and might thus distort the shape of the power spectrum. It also complicates comparisons between the measured power spectrum and theoretical predictions.

However, the angular power spectrum remains a powerful diagnostic tool, for example in the evaluation of the two methods used to eliminate large-scale structure described in Section 4.1.

4.4. Study of the Region A Excess

The study of Region A in Milagro data showed that the spectrum of the cosmic-ray flux in this region is harder than the isotropic cosmic-ray flux, with a possible cut-off around 10 TeV. At this point, a detailed study of the energy dependence of the flux in the excess regions with HAWC is not possible. Energy estimators based on the tank signal as a function of distance to the shower core are currently being developed, but these techniques will only reach their full potential with data from the complete 300-tank detector. Here, we perform a study based on a simple energy proxy that is based on the number of PMTs in the event and the zenith angle of the cosmic ray. In Fig. 9, we show the median cosmic-ray energy as a function of these two parameters, based on simulations. As expected, for a fixed number of PMTs, the median energy rises with zenith angle, as the shower has to traverse a larger integrated atmospheric depth.

Based on this plot, we identify 7 bins in median energy given by $(1.7^{+6.6}_{-1.3})$ TeV, $(3.2^{+10.9}_{-2.4})$ TeV, $(5.6^{+14.2}_{-3.9})$ TeV, $(8.4^{+20.3}_{-5.9})$ TeV, $(9.8^{+24.8}_{-6.7})$ TeV, $(14.1^{+28.7}_{-9.9})$ TeV, and $(19.2^{+32.3}_{-13.3})$ TeV, respectively. We define Region A as all pixels within a radius of $10°$ about the center at $(\alpha, \delta) = (60.0°, -7.1°)$. The relative intensity of the cosmic-ray flux in Region A is then obtained using the sum of all the angular bins in this region, for the 7 median energy bins. To check the technique we also use the amplitude of a two-dimensional Gaussian fit to the relative intensity map. Since the relative intensity of the excess as a function of radial distance to the center is relatively flat near the center, the methods give similar results.
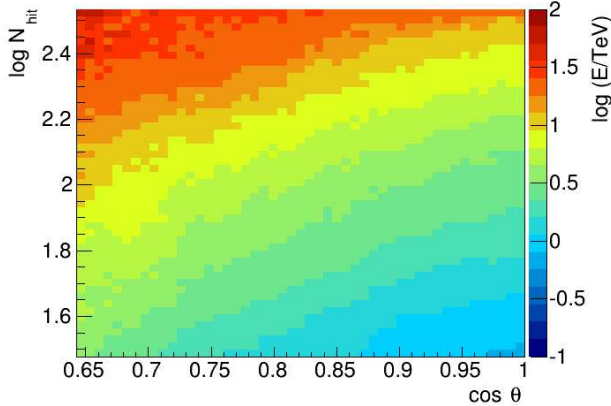
Figure 9. Median energy as a function of the number of triggered PMTs in the event, $N_{\rm hit}$, and the cosine of the zenith angle θ of the incident cosmic ray, from simulation.
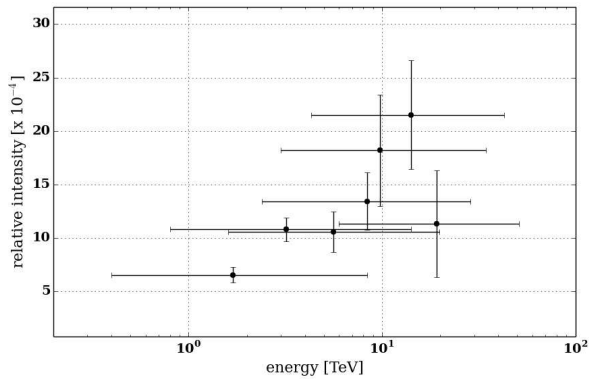

Figure 10. Spectrum of Region A in relative intensity in different energy proxy bins. The energies of the data were determined from Fig. 9. The error bars on the median energy values correspond to a 68% containing interval.

The relative intensity of the flux in the excess regions is plotted as a function of energy in Fig. 10. The abscissae show the median energy of each of the 7 bins, and the error bars correspond to the 68% containing interval of each bin. Despite the considerable overlap in energy between the bins, the analysis is sufficient to confirm that the energy spectrum of Region A is harder than the isotropic cosmic-ray spectrum.

We estimate the statistical significance of the hard spectrum in Region A by comparing the slope of a linear fit of δI versus $\log{(E)}$ in Fig. 10 to similar fits performed at many random locations in the field of view. These locations excluded the 15° circle centered on Regions A, B, and C. The distribution of slopes for the random locations follows an approximately Gaussian distribution centered at zero with a width of 1.2×10^{-4}. The slope at the position of Region A is $(4.5 \pm 1.0) \times 10^{-4}$, $3.8\,\sigma$ away from the mean.

The relative intensity of Region A is plotted in several energy bins in Fig. 11. The four highest energy bins from Fig. 10 have been combined to boost the statistics of the highest-energy plot. The location of the centroid of Region A reported by Milagro is plotted as a square marker. The data indicate that Region A changes in intensity and shape as a function of energy. In the bin with the lowest median energy, HAWC observes no sig-

nificant excess at the location of the Milagro centroid. As the median energy increases, the relative intensity of the excess observed in HAWC increases near the Milagro centroid. In the two bins of highest median energy, both measurements agree within uncertainties.

In their study of the energy dependence of the excess, the ARGO-YBJ collaboration observed a similar effect (Bartoli et al. 2013). The ARGO-YBJ analysis splits Region A in two parts, an upper part roughly coinciding with the brightest area in the Milagro map, and a lower part coinciding with the HAWC excess. At low energies, the lower part dominates, but as the energy increases the upper region becomes as bright as the lower region.

The study of the morphology and relative intensity of all excess regions as a function of energy will be continued with more data in the near future. The complete HAWC array will also have an improved energy resolution which will allow for a cleaner binning of data as a function of energy.

5. CONCLUSIONS

Using 4.9×10^{10} events recorded with partial HAWC configurations of 95 and 111 water-Cherenkov detectors we have observed a significant small-scale anisotropy in the arrival direction distribution of cosmic rays in the TeV band. The observations are largely in agreement with previous measurements of the anisotropy in the Northern Hemisphere. The sky map shows three regions of significantly enhanced cosmic-ray flux. The two most significant excess regions (Regions A and B) coincide with regions that have also been observed with the Milagro (Abdo et al. 2008), Tibet ASγ (Amenomori et al. 2005), and ARGO-YBJ experiments (Bartoli et al. 2013). Discrepancies between experiments in the location and the relative intensity of the excess regions may be due to the presence of unaccounted energy effects in the anisotropy. We also confirm the presence of a third region of cosmic-ray excess (Region C) which is not present in Milagro data, but was recently observed with ARGO-YBJ (Bartoli et al. 2013).

Applying an energy estimator that is based on the number of PMTs in the event and the zenith angle of the cosmic ray, we also study the energy dependence of the relative intensity in the region of the most significant cosmic-ray excess (Region A). We find that the spectrum in this region is harder than the isotropic cosmic-ray spectrum, in agreement with previous observations by Milagro and ARGO-YBJ.

General features of the cosmic-ray arrival direction distribution in the northern sky are also present in the southern sky, where the IceCube neutrino observatory is currently the only experiment contributing to cosmic-ray measurements in this energy band. A combined analysis of data from both hemispheres, with special attention to the small declination range where the cosmic-ray sky is visible (at large zenith angles) with both IceCube and HAWC will be performed in the near future. Since HAWC observes almost all charged secondary particles in air showers and IceCube can observe only the muonic component that reaches the detector after about a mile of ice, a comparison of data in the overlap region might also give some insight into possible systematic effects.
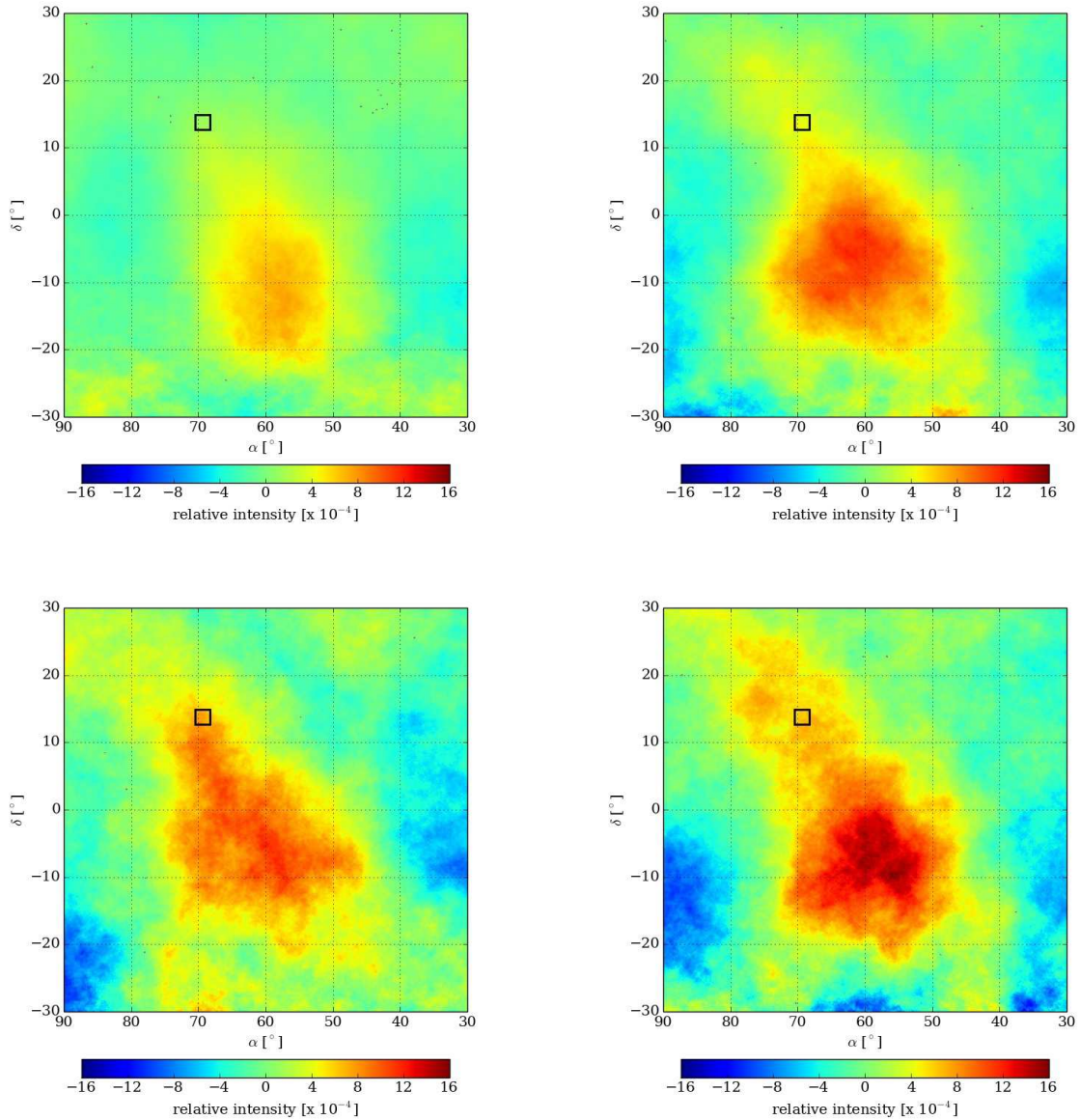
Figure 11. Relative intensity of Region A for 4 different energy proxy bins. The square mark denotes the location of the centroid of Region A as reported by Milagro ($\alpha = 69.4$, $\delta = 13.8$). The median energy of the data in each plot is $1.7^{+6.6}_{-1.3}$ TeV *(top left)*, $3.2^{+10.9}_{-2.4}$ TeV *(top right)*, $5.6^{+14.2}_{-3.9}$ TeV *(bottom left)*, and $14.1^{+28.7}_{-9.9}$ TeV *(bottom right)*.

REFERENCES

Aartsen, M., et al. 2013, Astrophys.J., 765, 55
Abbasi, R., et al. 2010, Astrophys. J., 718, L194
—. 2011, Astrophys.J., 740, 16
—. 2012, Astrophys.J., 746, 33
Abdo, A. A., et al. 2008, Phys. Rev. Lett., 101, 221101
—. 2009, Astrophys. J., 698, 2121
Abeysekara, A., et al. 2013a, Astropart.Phys., 50-52, 26
Abeysekara, A., et al. 2013b, in Proc. 33rd ICRC, Rio de Janeiro, Brazil, arXiv:1310.0074 [astro-ph.IM]
Abeysekara, A., et al. 2013c, in Proc. 33rd ICRC, Rio de Janeiro, Brazil, arXiv:1310.0071 [astro-ph.HE]
Aglietta, M., et al. 2009, Astrophys. J. Lett., 692, L130
Agostinelli, S., et al. 2003, Nucl. Instrum. Meth., A506, 250
Ahlers, M. 2014, Phys.Rev.Lett., 112, 021101
Amenomori, M., et al. 2005, Astrophys. J., 626, L29
Atkins, R. W., et al. 2003, Astrophys.J., 595, 803
Bartoli, B., et al. 2013, Phys.Rev., D88, 082001

Blasi, P., & Amato, E. 2012, JCAP, 1201, 011
Chon, G., et al. 2004, Mon. Not. Roy. Astron. Soc., 350, 914
de Jong, J. 2011, in Proc. 32nd ICRC, Beijing, China
Desiati, P., & Lazarian, A. 2013, Astrophys.J., 762, 44
Di Sciascio, G. 2013, EPJ Web Conf., 52, 04004
Drury, L. 2013, in Proc. 33rd ICRC, Rio de Janeiro, Brazil
Efstathiou, G. 2004, Mon.Not.Roy.Astron.Soc., 349, 603
Erlykin, A. D., & Wolfendale, A. 2006, Astropart.Phys., 25, 183
Giacinti, G., & Sigl, G. 2012, Phys.Rev.Lett., 109, 071101
Gorski, K., Hivon, E., Banday, A., Wandelt, B., Hansen, F., et al.
    2005, Astrophys.J., 622, 759
Guillian, G., et al. 2007, Phys. Rev. D, 75, 062003
Harding, J. P. 2013, arXiv:1307.6537

Heck, D., et al. 1998, CORSIKA: A Monte Carlo Code to
    Simulate Extensive Air Showers, Tech. Rep. FZKA-6019
Li, T.-P., & Ma, Y.-Q. 1983, Astrophys.J., 272, 317
Perez-Garcia, M. A., Kotera, K., & Silk, J. 2014,
    Nucl.Instrum.Meth., A742, 237
Pohl, M., & Eichler, D. 2013, Astrophys.J., 766, 4
Santander, M. 2013, PhD Thesis, University of
    Wisconsin-Madison
Schwadron, N., et al. 2014, Science, 343, 988
Sveshnikova, L., Strelnikova, O., & Ptuskin, V. 2013,
    Astropart.Phys., 50-52, 33
Szapudi, I., Prunet, S., Pogosyan, D., Szalay, A. S., & Bond, J. R.
    2001, Astrophys. J., 548, L115